The Rossby Adjustment Problem in a Rotating, Stratified Channel, with and without Topography

WILLIAM W. HSIEH

School of Mathematics, University of New South Wales, Kensington, NSW 2033, Australia

ADRIAN E. GILL

Department of Applied Mathematics and Theoretical Physics, University of Cambridge, Cambridge CB3 9EW, U.K.

(Manuscript received 15 June 1983, in final form 18 October 1983)

ABSTRACT

Some numerical experiments on geostrophic adjustment in a stratified channel were carried out, partly to test the use of an ocean general circulation model (GCM), and partly to elucidate the dynamical effects of sloping bottom topography on the adjustment at different latitudes. Interesting dynamical effects include the release of potential energy through shelf waves, the nonlinear generation of barotropic flow by a baroclinic Kelvin wave and the nonlinear generation of shelf waves with approximately half the inertial frequency by internal Poincaré waves of near-inertial frequency. Problems that inevitably occur in the use of GCMs were also highlighted.

1. Introduction

The Rossby adjustment problem examines how pressure and velocity distributions in the atmosphere and ocean undergo adjustment towards geostrophic equilibrium, starting from an original state of non-equilibrium. In an atmosphere and ocean full of disturbances and fronts, the Rossby adjustment problem tries to elucidate the complicated dynamics by studying the adjustment to equilibrium with the simplest possible system subjected to an idealized initial perturbation. Some pertinent questions raised are: what waves are generated during the adjustment process; how much potential energy can be converted to kinetic energy; and what is the final equilibrium state?

Following the original study by Rossby (1937, 1938), Gill (1982, p. 191) illustrates the approach to equilibrium of a shallow homogeneous unbounded fluid, initially at rest in a rotating system, but with a step-discontinuity in the surface elevation. Imagine a thin dam with different water levels on the two sides, collapsing at time $t = 0$, generating a gravity-wave front to either side. If the fluid is nonrotating, the final state has a level surface, i.e., the potential energy in the initial surface elevation has been converted completely to kinetic energy (Gill, 1982, p. 110). With a rotating fluid, however, the final surface elevation is not level—the initial step-discontinuity has only been smoothed to a width characterized by the Rossby radius of deformation (Gill, 1982, p. 194). Thus, of the infinite amount of potential energy available from the original surface discontinuity, only a finite amount can be converted to kinetic energy in a rotating fluid.

The effects of vertical sidewalls on the adjustment process are studied by Gill (1976; also 1982, p. 385), where in addition to Poincaré waves, coastally trapped Kelvin waves are present. A steady coastal current is established after the passage of the Kelvin wave front.

The Rossby adjustment problem is useful as a guide to how buoyancy effects can influence the ocean circulation. For instance, suppose a dam were placed between Greenland, Iceland and Scotland to isolate the Norwegian–Greenland Sea from the rest of the North Atlantic. The Norwegian–Greenland Sea water would presumably be colder than that in the North Atlantic; so what would happen if the dam were suddenly removed? Presumably, warm water from the Atlantic would flow into the Norwegian–Greenland Sea, but the Rossby adjustment problem for a channel teaches us that the flow would only occur against the eastern boundary, i.e., the warm water would flow in as a boundary current past the north of Scotland and up the Norwegian coast. This transient problem in itself does not say how buoyancy effects will act in the long term, but gives some very useful ideas.

The above experiment with a dam from Greenland to Scotland along the sill was actually performed numerically using a 1° grid resolution. To understand the results of that model, however, some simpler numerical experiments on geostrophic adjustment in a channel were performed and these are the ones reported here. The purpose was to see *how shelf topography*

affects the adjustment process. The effect must depend on the ratio of the Rossby radius to the shelf width; so four experiments were carried out to demonstrate such effects. These consisted of having channels with and without topography and comparing the results for channels at low and high latitudes. The $3\frac{1}{2}°$-latitude-wide channels were oriented east–west, with denser water on the eastern half partitioned off by an initial "dam" placed vertically across the midpoint of the channel. The change of latitude was meant to show the effect of changing the Rossby radius (which is proportional to the inertial period). However, it also showed up a numerical problem because the Rossby radius was not resolved in the high-latitude cases, the grid resolution being deliberately chosen to be like those in the larger model. Nonlinear effects also turned out to be important and led to some interesting dynamics. Another feature of the numerical cases not present in the earlier studies is the large lateral eddy coefficients, particularly the one associated with momentum. This quickly removes energy from the boundary current and leaves it to approach a steady-state configuration. Specifications for the four model runs are given in Table 1.

2. Channel with flat bottom

The first run, Experiment 1A, is the high-latitude, flat-bottom channel. Fig. 2a shows the density change (from the initial state) at the second level at the end of 20 days, while Fig. 2b shows the velocity field at the top level. The presence of coastally trapped waves is evident in both figures. The waves are baroclinic, as the velocity at the bottom level (not shown) is directed opposite to those at higher levels. The manifestation of the trapped waves in the density field is strongest at intermediate depth (the third level), whereas in the velocity field, the manifestation is weakest at this depth. This agrees with the vertical structure of the first baroclinic mode, where (for an ocean with constant buoyancy frequency) the density perturbation and velocity profiles have respectively maximum and minimum amplitudes at an intermediate depth.

TABLE 1. Common features of the runs: width of channel, $3\frac{1}{2}°$ of latitude; half-length of channel, 9° of longitude (so the high-latitude channel is actually shorter). Grid is 1°of longitude × $\frac{1}{2}°$ of latitude, with four vertical levels as shown in Fig. 1. Initial density distribution in the eastern and western halves is given in Fig. 1. The Semtner (1974) version of the Bryan–Cox model was used. Starting from an initial state of rest with density discontinuity at the "dam", the model was relaxed without forcing for 20 days. Lateral eddy viscosity $\nu = 5 \times 10^3$ m^2 s^{-1}, lateral eddy diffusivity = 2×10^3 m^2 s^{-1}, vertical eddy viscosity and diffusivity both = 10^{-4} m^2 s^{-1}, depth of channel = 2000 m. Variations between the runs are given below.

Case	Location of channel (°North)	Bottom topography
1A	57–60	Flat
1B	7–10	Flat
2A	57–60	Shelf
2B	7–10	Shelf

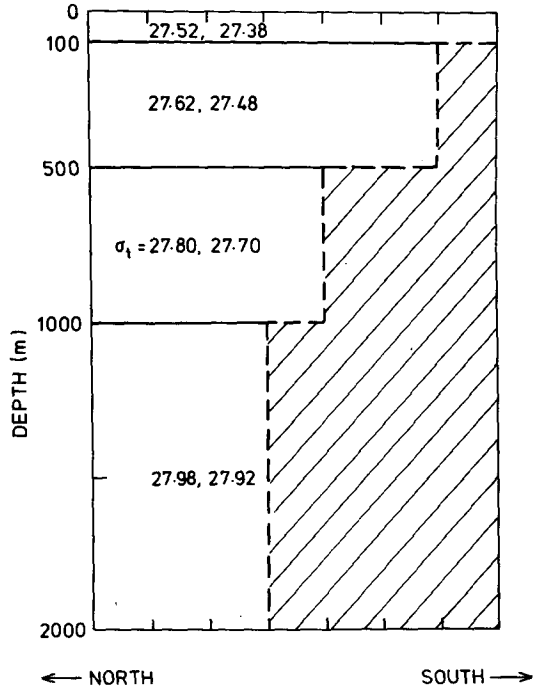

FIG. 1. North–south vertical section of the channel. The two values of initial density (σ_t) given at each level are those east and west of the front respectively. The dashed contour shows the bottom topography used in the experiments of Section 3. The north–south grid-spacing is ½° latitude.

In this coarse-grid model, the offshore grid-spacing of ½° latitude (55 km) is much wider than the baroclinic Rossby radius R (~20 km). This finite difference effect, together with the large lateral viscosity needed for computational stability, produces a baroclinic Kelvin wave with a much greater width than R and a much lower phase speed c. In other words, the properties of the boundary current seen in Fig. 2 are, unfortunately, strongly dependent on the grid spacing and therefore somewhat artificial. With smaller grid-spacing, the same vertical structure would be expected, but the boundary currents would be much narrower. Effects of lateral and vertical viscosity on the Kelvin wave have been studied by Davey *et al.* (1983) and the Kelvin wave behavior in finite-difference numerical models, by Hsieh *et al.* (1983).

The behavior of the model with time, shown in Fig. 3, indicates that the changes with time at the end of 20 days are rather slow, so the fields in Fig. 2 are in a quasi-steady state. For discussion, we write the governing momentum equations in Cartesian form, with x oriented eastward (alongshore) and y, northward (offshore).

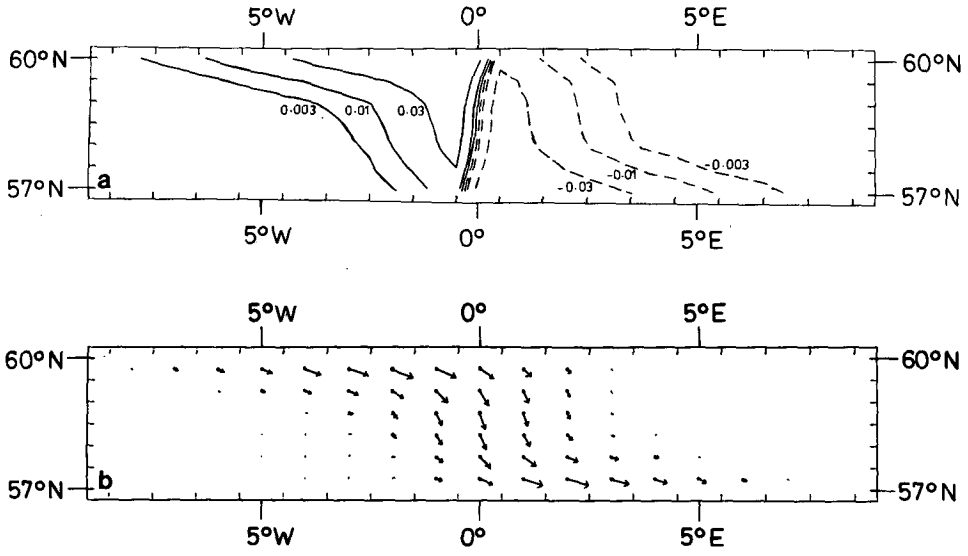

FIG. 2. (a) Density change (from initial state) at the second level (300 m) and (b) horizontal velocity field at the top level (50 m), at the end of 20 days in Experiment 1A. In (a) the σ_t contour values increase by a factor of $10^{1/2}$ between adjacent contours (a convention used for all figures), i.e., the contour label 3 is really $10^{1/2}$. Dashed contours indicate negative values (i.e., decrease in density). In (b), the velocity scale is 5 cm s^{-1} for a vector of length equal to the N–S grid spacing. The inward tick marks along the axes indicate the grid for temperature, salinity and streamfunction, while the velocity grid points are located in between. The initial front was located along 0°E.

$$\frac{Du}{Dt} - fv = -\frac{1}{\rho_0} p_x + \nu(u_{xx} + u_{yy}) + \kappa u_{zz}, \quad \text{(1a)}$$

$$\frac{Dv}{Dt} + fu = -\frac{1}{\rho_0} p_y + \nu(v_{xx} + v_{yy}) + \kappa v_{zz}, \quad \text{(1b)}$$

$$p_z = -\rho g, \quad \text{(1c)}$$

where D/Dt denotes the Lagrangian derivative and ν and κ, the lateral and vertical viscosities. After the passage of the wave front, a steady state with no alongshore pressure and density gradients is achieved in the inviscid theory. In this run, the balance in (1a) near the coast appears basically to be the finite difference version of

$$p_x = \rho_0 \nu u_{yy}, \quad (2)$$

while (1b) stays mainly geostrophic, i.e.,

$$-p_y = \rho_0 f u. \quad (3)$$

These combine to give

$$p_x + \frac{\nu}{f} p_{yyy} = 0. \quad (4)$$

So if the y-scale were $R = c/f$, the x-scale would be $R^3 f \nu^{-1} = c^3 \nu^{-1} f^{-2}$. However, since the y-scale depends strongly on the grid spacing, so does the x-scale.

Figure 3 shows the velocity u along the south coast, where the clearly visible asymmetry between east and

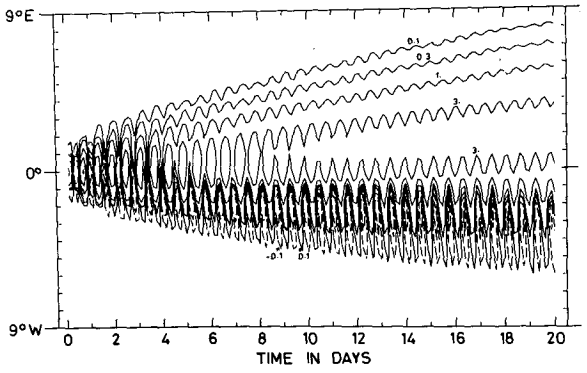

FIG. 3. Space–time contour plot of the alongshore velocity u (at top level) along the south coast in Experiment 1A.

west may be ascribed to the Kelvin wave propagating only eastward. (It is best to look at say the 1 cm s^{-1} contour rather than the envelope of the contours). The wave front moves out much slower than its theoretical speed c because of the numerical effects (Hsieh *et al.*, 1983). Note also the inertial oscillations which are part of the adjustment process. This case will not be examined further because of the numerical effects.

For Experiment 1B, we place the channel at low latitudes, 7–10°N, where R is now ~120 km and much wider than the offshore grid spacing Δ (55 km). Except for the change in latitude, all other parameters (including stratification) are the same as in the high-latitude case.

Figure 4, the space–time contour plot of u along the southern coast, is the low-latitude counterpart of Fig. 3. Here the inertial period is much longer, and the inertial oscillations appear to radiate internal waves westward. On the eastern side, the propagating Kelvin-wave front is seen. Because of the smaller ratio of Δ/R (i.e., better offshore resolution), the baroclinic Kelvin wave should travel faster here than in Experiment 1A, as predicted theoretically by Hsieh *et al.*, (1983). Indeed, the Kelvin-wave front has reached the eastern boundary by day 10 in Fig. 4, whereas in Fig. 3, it has not reached the boundary by day 20.

Figures 5a, b, when compared with Figs. 2a, b, show a much wider coastal jet and associated density field—a manifestation of the much larger R at low latitudes. The alongshore density gradient is much weaker (or the alongshore decay scale is much larger) than in Fig. 2a, tentatively agreeing with our finding from (4) that the alongshore scale is $c^3\nu^{-1}f^{-2}$, i.e., proportional to f^{-2}.

The transport streamfunction ψ, defined by

$$\psi_y = -\int_{-h}^{0} u\,dz, \quad \psi_x = \int_{-h}^{0} v\,dz, \tag{5}$$

where h is the depth, is negligibly small in Experiment 1A. But in 1B, barotropic flow develops after the passage of the baroclinic Kelvin-wave front, as manifested in the ψ-field at day 5 and day 20 (Figs. 6a and b). The interesting three-cell circulation pattern can also be detected in the space–time contour plot of ψ in Fig. 7, where in addition, we note the slow westward drift of the pattern at a speed of ~5.6 cm s^{-1}. It thus appears that the baroclinic Kelvin wave transfers energy to a barotropic Rossby wave.

The equations governing the generation of barotropic flow by non-linear effects can be derived as follows. Let

$$(u, v, p) = (\bar{u}, \bar{v}, \bar{p}) + (\hat{u}, \hat{v}, \hat{p}), \tag{6}$$

where the overbar represents the depth-averaged (barotropic) part and the caret signifies the remaining baroclinic part. Neglecting viscous terms in (1a) for convenience, the depth-averaged form is

$$\frac{D}{Dt}\bar{u} - f\bar{v} + \frac{1}{\rho_0}\bar{p}_x = -(\overline{\hat{u}\hat{u}})_x - (\overline{\hat{v}\hat{u}})_y, \tag{7}$$

where D/Dt is the derivative following the depth-averaged motion. This equation shows how baroclinic motion can generate barotropic flow by nonlinear ef-

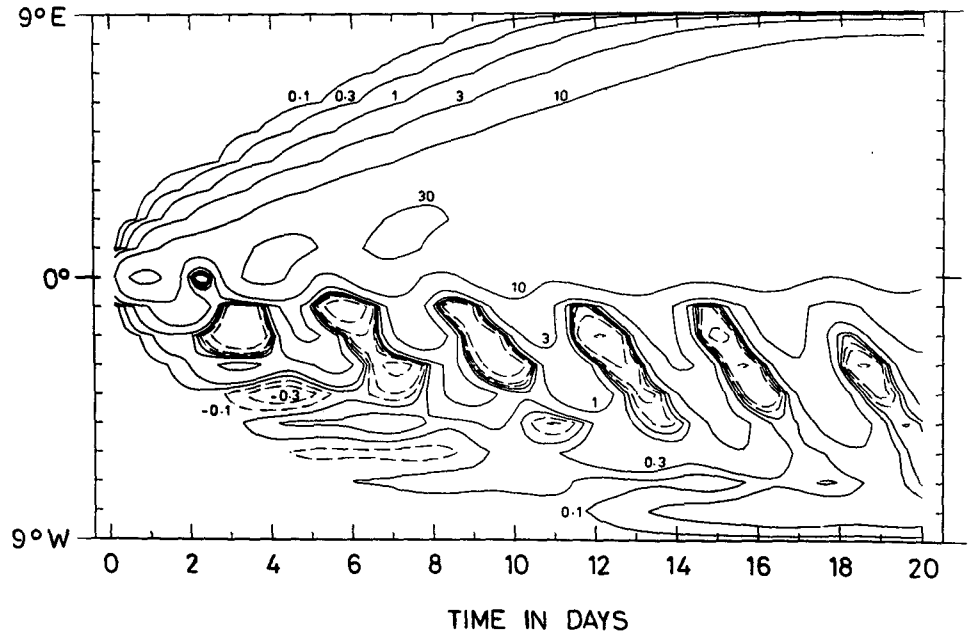

FIG. 4. As in Fig. 3 but in Experiment 1B (low latitudes).

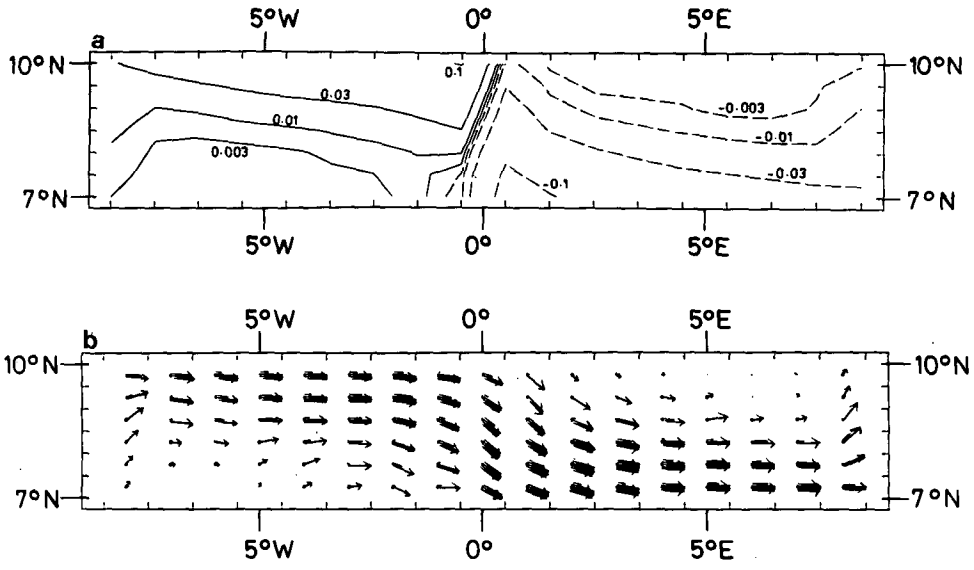

FIG. 5. (a) Density change at the second level (in σ_t units) and (b) horizontal velocity field at the top level at the end of 20 days in Experiment 1B (low latitudes). The velocity scale remains 5 cm s^{-1}; repeated lines are drawn when the speed exceeds 5 cm s^{-1}.

fects. To confirm the nonlinearity experimentally, case 1B was repeated with half the amplitude (i.e., half the strength of the initial front) and the streamfunction was found to drop by a factor of 4.

Consider now an idealized case of a constant buoyancy-frequency fluid in which a long, first baroclinic wave is traveling along the boundary. A wave moving eastward along the southern boundary has the form

$$\frac{\hat{p}}{\rho_0} = e^{-y/R}P(x - ct)\cos(\pi z/H),$$

$$c\hat{u} = e^{-y/R}P(x - ct)\cos(\pi z/H), \quad \hat{v} = 0, \qquad (8)$$

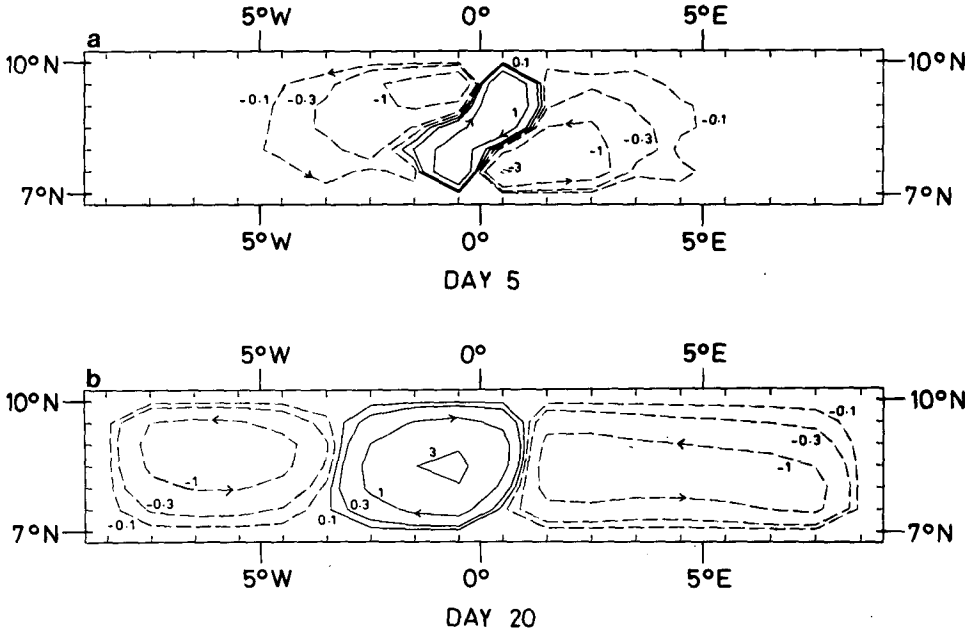

FIG. 6. The transport streamfunction ψ (in Sv) at (a) day 5 and (b) day 20 in Experiment 1B. Positive values (solid lines) and negative values (dashed lines) indicate anticyclonic and cyclonic circulation respectively.

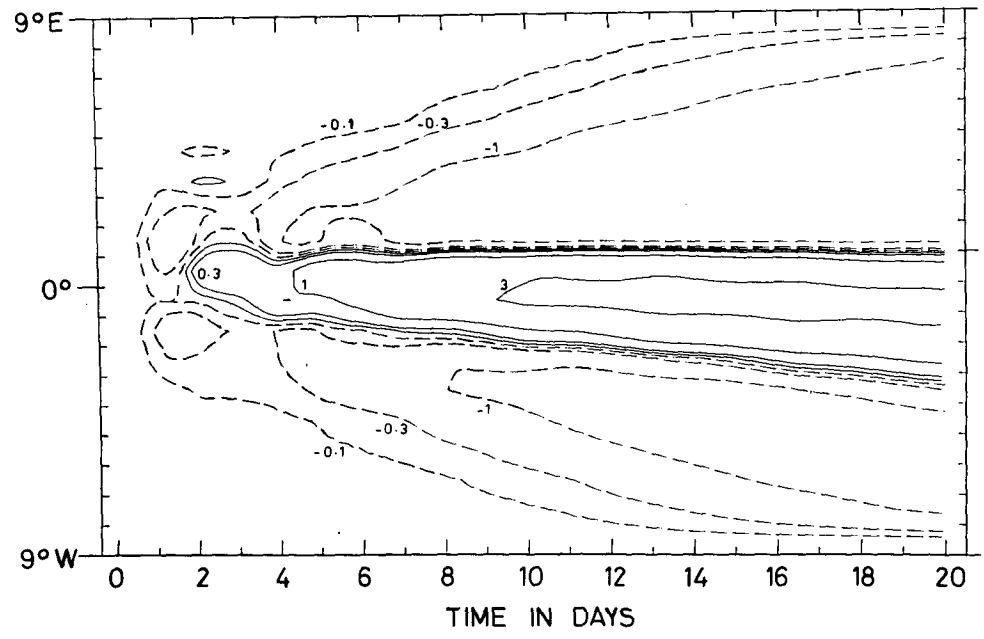

FIG. 7. Space–time contour plot of ψ along a constant latitude in midchannel in Experiment 1B. The development of the three-cell circulation pattern behind the propagating Kelvin-wave fronts can be seen as well as the slow westward drift of the entire pattern.

where P is a function that varies slowly compared with the scale of R and is zero ahead of the wave. The maximum density jump across the wave occurs at mid-depth, with the value

$$\Delta\rho = \frac{\pi P}{gh}. \tag{9}$$

Analogous to (7), a momentum equation for $\bar{v}$ can easily be found, with the right-hand side zero since $\hat{v} = 0$. Taking the curl of the $\bar{u}$ and $\bar{v}$ momentum equations (with $f = f_0 + \beta y$), we obtain

$$\frac{D}{Dt}(\psi_{xx} + \psi_{yy}) + \beta\psi_x = h(\overline{\hat{u}^2})_{xy}, \tag{10}$$

where the homogeneous equation is the familiar one for barotropic Rossby waves. The linear long-wave approximation to (10) is

$$\psi_{yyt} + \beta\psi_x = h(\overline{\hat{u}^2})_{xy}, \tag{11}$$

which can be integrated once to give

$$-c\psi_{yy} + \beta\psi = h(\overline{\hat{u}^2})_y = -\frac{h}{Rc^2}\, e^{-2y/R}P^2. \tag{12}$$

This satisfies the condition that ψ is zero ahead of the wave.

Equation (12) can easily be solved exactly, but in the present case the beta-term is small (it becomes important nearer the Equator). Neglecting the beta-term, the solution is

$$\psi = \frac{hR}{4c^3}\, P^2\left(e^{-2y/R} - 1 + \frac{y}{b}\right), \tag{13}$$

where b, the width of the channel is assumed long compared with $\frac{1}{2}R$ (a good approximation here). This solution gives a negative ψ-field (whatever the sign of the baroclinic wave) with a front moving eastwards at speed c and coinciding with the baroclinic wave front. There is a strong eastward current on the southern boundary and a weaker return flow in the rest of the channel. These features match the results shown in Fig. 6 very well. The westward moving Kelvin wave on the northern boundary produces a similar effect.

The effect can easily be explained by examining the relevant equations. The right-hand side of (7) can be regarded as proportional to stress acting on the barotropic flow, analogous to the Reynolds stress of turbulent flow, except here we have a *depth*-averaged term rather than a *time*-averaged term. The curl of this stress generates vorticity as shown by (10). The effect can be quite important in other contexts as well, e.g., in driving barotropic contributions to western boundary currents in circulation experiments such as those of Gill and Bryan (1971).

In the present case, $\overline{\hat{u}^2}$ goes from positive values in the coastal wave to zero ahead of the wave, giving a tendency [see Eq. (7)] to accelerate the barotropic flow in the direction the wave is traveling. Averaged across the width of the channel, however, there can be no acceleration by continuity, so the width-averaged $\overline{\hat{u}^2}$ is balanced by a pressure change, i.e., there is a Ber-

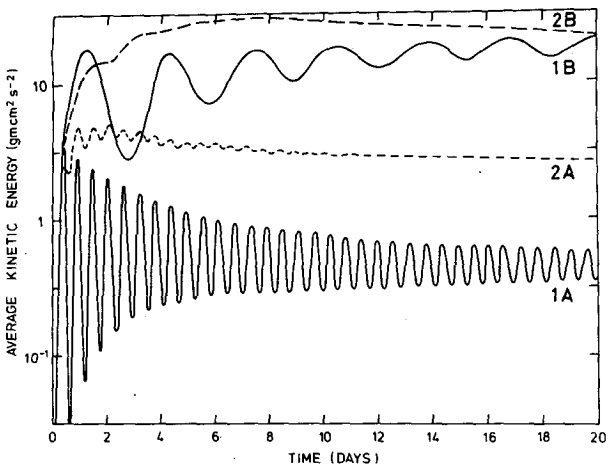

FIG. 8. Average kinetic energy (per unit volume) in the channel for the four numerical experiments (1A and 1B, without topography at high and low latitudes and 2A and 2B, their counterparts with shelf topography). The average kinetic energy is the total kinetic energy in the channel divided by the volume. The curves demonstrate that more potential energy from the initial front is converted to kinetic energy when the adjustment takes place at low latitudes or in the presence of a sloping bottom.

noulli balance with a reduced pressure where there is a wave. The differences of $\hat{u}^2$ from its width-averaged value give the accelerations which generate the observed flow.

Note that by (9) and (13), for a given $\Delta\rho$, the strength of the barotropic flow is proportional to R. Therefore, the effect will be much stronger at low latitudes, as found in the present experiments.

The above model shows how barotropic vorticity is generated at the Kelvin-wave front, but does not take into account the flow in the whole of the basin. The source terms in (7) are, in fact, zero when integrated over the whole of the basin and the same holds true for the other component of horizontal momentum. As the total vorticity generation is zero, the cyclonic gyres generated by the passage of the waves must be accompanied by an anticyclonic gyre in the neighborhood of the original front. This explains the three-cell circulation seen in Fig. 7. As time goes on, the cells gradually propagate westward because of the beta-effect.

The average kinetic energy per unit volume in the channel as a function of time is shown in Fig. 8. Experiments 1A and 1B have initial fronts of the same strength, but the amount of potential energy converted to kinetic energy is very much larger in 1B. The inertial oscillations are manifest in both cases, though they are weaker in 1B.

3. Channel with continental shelf

What happens to the adjustment process in the presence of bottom topography—such as a continental

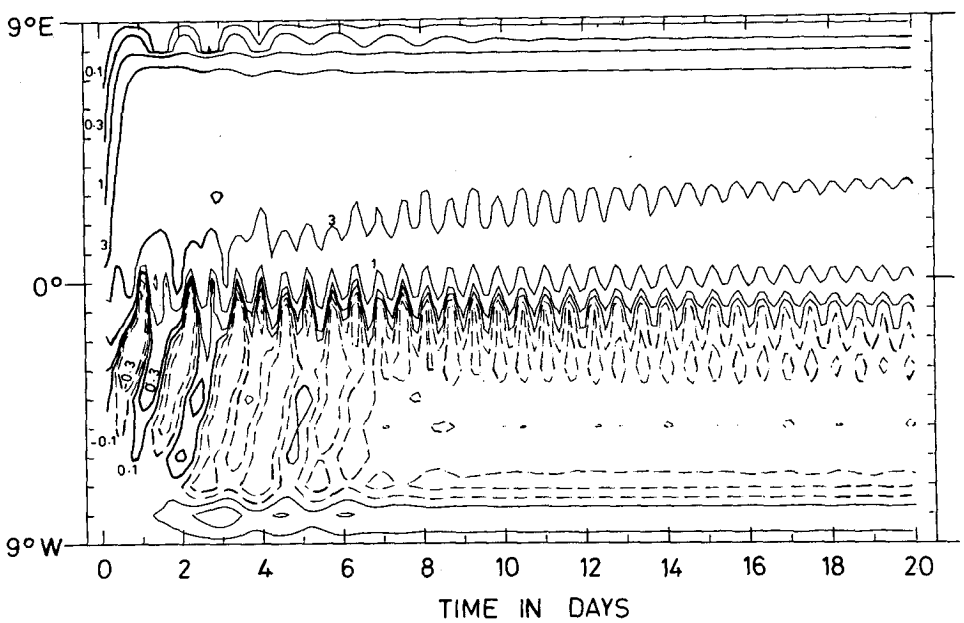

FIG. 9. Space–time contour plot of u (at top level) along the south coast in Experiment 2A (with continental shelf along south coast). On the eastern half, a shelf-wave front is seen to propagate rapidly, reaching the end within a day. A much slower baroclinic propagation with inertial oscillations superimposed follows at $\sim$10 km d^{-1}. On the western half, a short shelf wave (with group velocity opposite to its phase velocity) is generated subharmonically by the inertial oscillations about the original front, i.e., the phase is propagating eastward, the energy, westward and the period is twice the inertial period.

shelf? To find out, we repeat the numerical experiments at high and low latitudes, this time with a continental shelf along the southern boundary (Fig. 1).

Figure 9, the space–time contour plot of u along the coast in Experiment 2A (with channel at high latitudes), is to be contrasted with Fig. 3, its counterpart with no topography. On the eastern side, a shelf-wave front can be seen to propagate rapidly, reaching the end of the channel within a day (Fig. 9) and setting up a strong barotropic cyclonic circulation in the eastern half of the channel (Fig. 10a). The western half is not entirely quiet, however, as Fig. 9 reveals a wave radiated westward from the inertial oscillations about the original front. It is easily seen from Fig. 9 that this wave has twice the period of the inertial oscillations, has phase propagating eastward (but with lower phase speed than the shelf wave in the eastern half of the channel) and has energy propagating westward. Thus, a short shelf wave—with group velocity opposite to its phase velocity—is generated subharmonically from the inertial oscillations about the initial front. This short shelf wave is also manifested clearly in the streamfunction on the western part of the channel (Fig. 10a).

The most striking difference between this experiment and its flat-bottom counterpart is the tremendously asymmetric distribution of kinetic energy in the channel with topography. Here, the kinetic energy in the eastern half of the channel is several orders of magnitude larger than that in the western half. The asymmetry may be ascribed to the strong barotropic circulation that is quickly established on the eastern side after the passage of a shelf-wave front. The only shelf waves that can propagate to the west are short ones and they carry relatively little energy.

Figure 10b shows that by day 20, the cyclonic gyre has penetrated partly into the western half of the channel. At the same time, the density contours in Fig. 11 reveal that a baroclinic Kelvin wave has propagated westward along the northern boundary, as in the flat-bottom case (Fig. 2a). The contours in this part of the channel are practically identical, indicating that the Kelvin wave over the flat part of the channel is little affected by the presence of the shelf to the south. In contrast, the changes in the eastern half of the channel are strongly affected by topography. The most striking difference is the decrease in density seen in Fig. 11 at the eastern end. This is due to the downslope flow seen in Fig. 10 which entails a downward component and hence, carries light fluid downwards. In this way, the so-called "barotropic" or vertically integrated flow is releasing potential energy. Also, a baroclinic coastally trapped wave can be seen in the eastern half in Fig. 11 and in Fig. 9, where it propagates much slower than the shelf wave. The coastal alongshore velocity in Fig. 9 decreases after the passage of this eastward baroclinic wave.

We next examine how the shelf-wave front was generated from the initial density front. We neglect the viscous and nonlinear terms in (1) and write

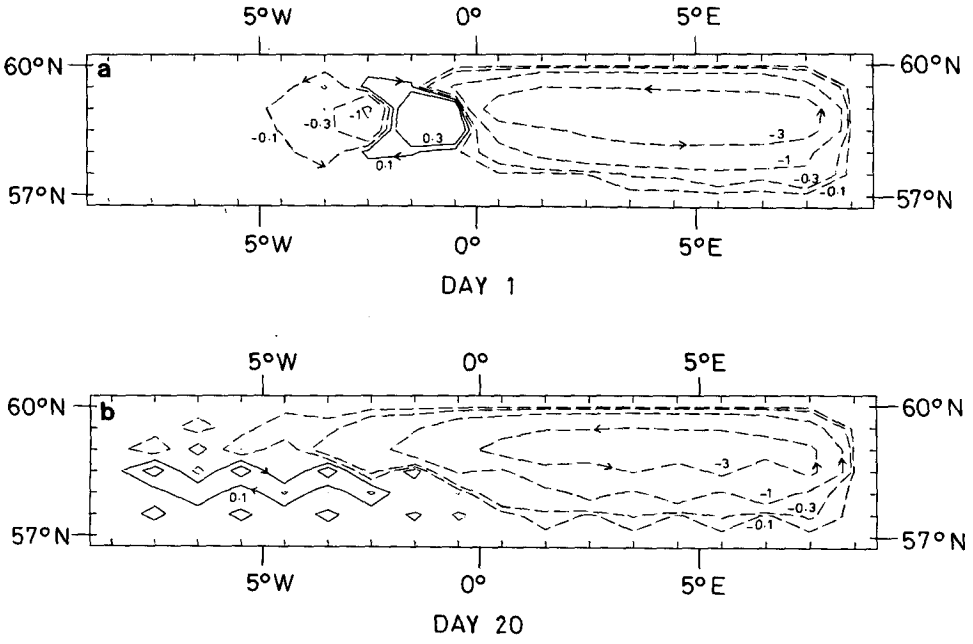

FIG. 10. The streamfunction ψ at (a) day 1 and (b) day 20 in Experiment 2A. At day 1, the shelf-wave front has already reached the end of the channel, and a strong cyclonic circulation is established in the eastern half of the channel whereas on the western half, only the short shelf-wave (manifested by the two vortices of opposite signs) can be seen.

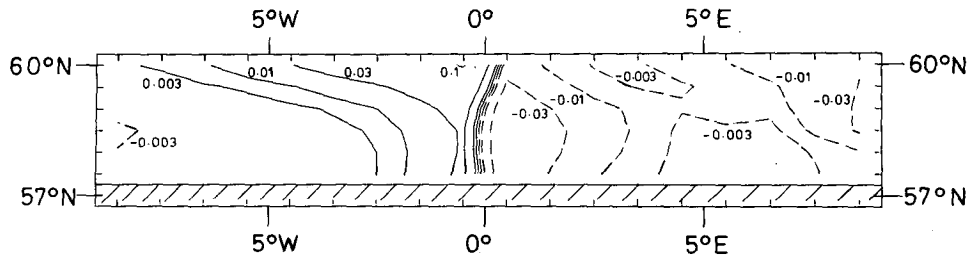

FIG. 11. The density change at level 2 at day 20 in Experiment 2A.

$$p(z) = p_s + \int_z^0 g\rho dz', \tag{14}$$

where p_s is the surface pressure from the rigid-lid. Following Semtner (1974), we depth-average (1a) and (1b), substitute in (5) and then take the curl of the two equations to get

$$\left(\frac{1}{h}\psi_{yt}\right)_y + \left(\frac{1}{h}\psi_{xt}\right)_x + \left(\frac{f}{h}\psi_x\right)_y - \left(\frac{f}{h}\psi_y\right)_x = \left[\frac{g}{\rho_0 h}\int_{-h}^0\int_z^0 \rho_x dz'dz\right]_y - \left[\frac{g}{\rho_0 h}\int_{-h}^0\int_z^0 \rho_y dz'dz\right]_x. \tag{15}$$

For our situation, we have $h = h(y)$, $(h' \equiv h_y)$ and $\rho = \rho(x, z)$, whereby (15) reduces to

$$\psi_{yyt} + \psi_{xxt} - \frac{h'}{h}(\psi_{yt} + f\psi_x) = \frac{gh'}{\rho_0}\left(-\frac{1}{h}\int_{-h}^0\int_z^0 \rho_x dz'dz + \int_{-h}^0 \rho_x dz'\right) = \frac{h'}{\rho_0}\left[\frac{1}{h}\int_{-h}^0 p_x(z)dz p_x(-h)\right], \tag{16}$$

where the two terms in the brackets represent the depth-averaged pressure gradient and the bottom pressure gradient in the alongshore direction respectively. Our choice of an initial step-discontinuity in density and a sudden "dam-break" can be modeled by

$$\psi_{yyt} + \psi_{xxt} - \frac{h'}{h}(\psi_{yt} + f\psi_x) = \frac{h'}{h\rho_0} X_0\delta(x)H(t)Y(y), \tag{17}$$

where $H(t)$ is the Heaviside step function, $\delta(x)$ is the Dirac delta function arising from differentiating the step discontinuity in density and X_0 is a constant and $Y(y)$ a function, both of which are determined from the initial density distribution by (16). Strictly speaking, the delta function on the right-hand side of (17) is appropriate only at the initial instant when the density step is sharp. However, the spread of the step is slow, as Fig. 11 shows, and the effect of this spread is ignored in the analysis below.

The term on the right-hand side of (17) represents a source of barotropic vorticity which can enhance transports in the western boundary layers in circulation models with shelflike topography (Holland, 1973). In the present context, the reason for the torque can be ascribed to the fact that the denser water tends to fall to the lowest possible level for a minimum potential energy configuration. In the presence of topography, horizontal motion may be required to reach the lowest level hence, a barotropic component to the flow.

Equation (17) is difficult to solve as written, but the dominant feature of the response, namely the propagation of a shelf wave to the east, is easily understood and fairly well modeled by taking the longwave approximation to (17), i.e., neglecting the ψ_{xxt} term. Then, following Gill and Schumann (1974), a solution can be found in the form

$$\psi(x, y, t) = \sum_n \phi_n(x, t)F_n(y), \tag{18}$$

$$Y(y) = \sum_n b_n F_n(y), \tag{19}$$

where $F_n(y)$ are the free shelf-wave eigenfunctions from the unforced problem. The equation for ϕ is then

$$c_n^{-1}\frac{\partial\phi}{\partial t} + \frac{\partial\phi}{\partial x} = -b_n\frac{X_0}{f\rho_0}\delta(x)H(t), \tag{20}$$

with c_n the phase speed of the nth mode shelf wave. The solution from Gill and Schumann (1974) is

$$\phi_n(x, t) = \phi_n\left(x_0, t - \frac{x}{c_n}\right) - \frac{b_n}{f\rho_0}X_0\int_{x_0}^x \delta(\xi)H\left(t + \frac{\xi - x}{c_n}\right)d\xi. \tag{21}$$

Choosing x_0 just west of the front, then $\phi_n(x_0, t) = 0$ for all t and

$$\phi_n(x, t) = -\frac{b_n}{f\rho_0}X_0 H\left(t - \frac{x}{c_n}\right). \tag{22}$$

Thus, the initial density front generates a series of shelf-wave fronts, each propagating up the coast at a

particular speed c_n. The steady-state circulation after the passage of all the fronts is

$$\psi = -\frac{1}{f\rho_0} X_0 \sum_n b_n F_n(y) = -\frac{1}{f\rho_0} X_0 Y(y). \quad (23)$$

In Fig. 9, only the first-mode shelf-wave front can be clearly seen.

Equation (23) provides an estimate for ψ of -7.0×10^6 m^3 s^{-1} (-7 Sv) in deep water, using $X_0Y(y)$ calculated from the initial density distribution by (16). This value compares very well with the observed ψ maximum of approximately -6 to -7 Sv along the middle of the channel.

An interesting feature of this problem is that the source of energy is potential, but the motion initially established is largely barotropic. Where is the release of potential energy taking place? With barotropic flow, this can only happen where the flow is across depth contours. In the above solution, this happens at each shelf-wave front, while in the solution shown in Fig. 10, it happens at the eastern end of the channel. The direction is such as to carry the relatively dense water of the eastern half "downhill" hence, the release of potential energy. Potential energy is also released near the location of the initial front, but this is harder to analyze.

The presence of a continental shelf changes the numerical situation of Experiment 2A even though it has the same resolution ratio Δ/R as Experiment 1A. The continental shelf width L now replaces the baroclinic Rossby radius R as the relevant offshore length scale. As the shelf is several grid spacings in width, the resolution ratio Δ/L in Experiment 2A is much better than the corresponding ratio Δ/R in Experiment 1A. Furthermore, the presence of the shelf introduces a quasi-geostrophic balance in (1a) where fv and $\rho_0^{-1}p_x$ are of comparable magnitude. In contrast, the Kelvin wave in Experiment 1A has negligible fv in (1a), and the only steady-state balance is between the pressure gradient and lateral viscosity terms in (2). Hence, the presence of a shelf in Experiment 2A not only improves the effective resolution, but also inhibits the viscosity-dominated dynamics of (2).

We turn next to the nonlinear generation of the subharmonic shelf wave by the inertial oscillations, as seen in Fig. 9. For the inertial oscillations, the currents are circularly polarized, with the lower current oscillating out of phase with the upper current in the water column. As the lower current moves on and offshore over sloping topography, vortices of opposite signs are generated alternately. However, this forcing at the inertial frequency cannot generate shelf waves directly, as shelf waves have frequency $\omega < f$. Instead, the energy transfer is via a nonlinear mechanism analogous to that used by Guza and Davis (1974) and Guza and Bowen (1975) to explain the excitation of edge waves by incoming swell. Two edge waves of frequency and wavenumber (ω_1, k_1) and (ω_2, k_1) can be excited resonantly by an incident wave of frequency ω_i and alongshore wavenumber k_i, if the following resonance conditions are satisfied:

$$\omega_1 + \omega_2 = \omega_i, \quad k_1 + k_2 = k_i. \quad (24)$$

Thus, edge waves of lower frequency than the incoming swell are generated. In particular, the most readily generated edge wave is the subharmonic edge wave, with

$$\omega = \omega_1 = \omega_2 = \frac{1}{2}\omega_i, \quad k = k_1 = k_2 = \frac{1}{2}k_i. \quad (25)$$

The excitation of the subharmonic edge wave by incoming swell is widely observed on beaches (see, e.g., Guza and Inman, 1975).

In our case, the forcing by the near-inertial oscillations, i.e., low-frequency internal Poincaré waves (with dispersion relation $\omega^2 = f^2 + k^2c^2$), generates the subharmonic shelf waves with $\omega \approx \frac{1}{2}f$, as illustrated in Fig. 12a. On the western half of the channel, only the short shelf wave with westward group velocity can appear. The long shelf wave with group velocity eastward, as its phase velocity, can also be excited, but it is much harder to detect as the background energy in the eastern half of the channel is very much greater than in the western half. However, near a boundary, the background energy drops, since the velocity must vanish at the boundary. Indeed, the contours near the eastern end of the channel in Fig. 9 display oscillations at twice the inertial period, thereby revealing the presence of the long subharmonic shelf wave. Because of the much greater difficulty involved in detecting the long shelf wave, it is not possible to conclude from our figures whether the short or the long subharmonic shelf wave has more energy. Another intriguing possibility is the true triad interaction involving both the long and short shelf waves, as illustrated in Fig. 12b.

Past studies of nonlinear energy transfer in shelf waves include those by Hsieh and Mysak (1980), where energy transfer between three shelf waves is examined and by Barton (1977) and Hsieh (1982), where the nonlinear generation of shelf waves by wind is proposed. In general, the observational evidence for nonlinear energy transfer in shelf waves is very limited compared to that available for edge waves and gravity waves. The interaction observed here, i.e., the transfer of energy from internal Poincaré waves of near-inertial frequency to shelf waves of subinertial frequency, does not appear to have been studied before. It is an intriguing mechanism because energy is transferred between first class waves (which require gravity as a restoring force) and second class waves (which require the earth's rotation). The two halves of the channel reveal surprizingly different outcomes in the contest between the linear mechanism [i.e., the one given by Eq. (16)] and the nonlinear mechanism in the gen-

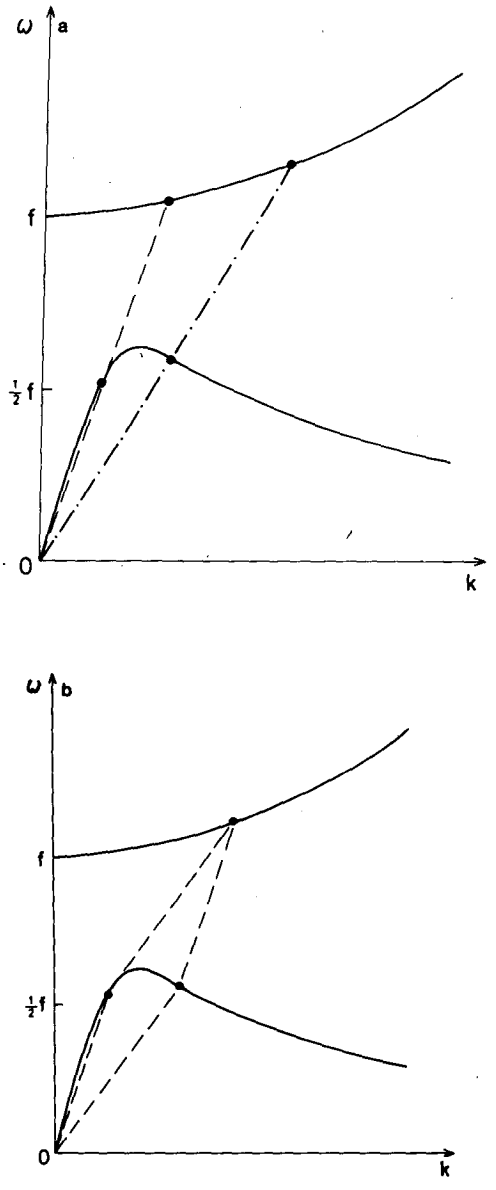

FIG. 12. Schematic dispersion diagrams illustrating the nonlinear transfer of energy between (internal) Poincaré waves and shelf waves. The upper dispersion curve ($\omega^2 = f^2 + k^2c^2$) is that for the first-mode internal Poincaré wave and the lower curve, that for a typical first-mode shelf wave. The nonlinear resonant mechanism based on Eq. (24) allows the excitation of shelf waves with $\omega_s \approx \frac{1}{2}f$ from near-inertial Poincaré waves with $\omega_p \approx f$. (a) Interactions involving one shelf wave and one Poincaré wave, satisfying $\omega_s = \frac{1}{2}\omega_p$, $k_s = \frac{1}{2}k_p$. The dashed line indicates interaction involving the long shelf-wave, while the dot-dashed line shows that involving the short shelf-wave. (b) Interaction involving three waves—a long shelf wave, a short shelf wave and a Poincaré wave.

eration of shelf waves. In the eastern half, the linear mechanism is undoubtedly stronger than the nonlinear mechanism (hence, the difficulty in observing the subharmonic long shelf wave). In contrast, the non-linear mechanism dominates over the linear one in the western half.

Experiment 2B is a repeat of Experiment 2A at low latitudes. Fig. 13 when compared with Fig. 9, its counterpart at high latitudes, shows a much slower eastward-propagating shelf-wave front and much weaker inertial oscillations. The short shelf wave can still be detected, though this time it has a much slower phase speed c (as seen from the small slope in the contours) and hence, a much shorter wavelength. The drop in c is expected because the phase speed of shelf waves tends to be directly proportional to f [see, e.g., the dispersion relation for a step-shelf of LeBlond and Mysak, 1978, Eq. (25.61)]; thus, c diminishes with decreasing latitude.

The first mode for our channel can be calculated approximately by fitting the depth profile

$$H = \begin{cases} 0.1 \exp(y/80), & 0 < y < 240 \\ 2.0, & 240 < y < 390, \end{cases}$$

where H and y are in km. The solution is easily found, as in Section 5 of Gill and Schumann (1974), giving

$$c/f = 86 \text{ km}.$$

This gives $c = 10$ m s^{-1} for the high-latitude channel and 1.8 m s^{-1} for the low-latitude channel, in good agreement with the numerical results.

The barotropic flow for the low-latitude case at days 1 and 20 is shown in Fig. 14 for comparison with Fig. 10. Again, the flow is much stronger in the eastern half. However, the relative slowness of the shelf-wave propagation at low latitudes is evident. If the waves moved rapidly out, as at high latitudes, ψ would be expected by (23), to have 6 times the value it had in case 2A, 6 being the ratio of the values of f. However, the maximum observed value is only -17 Sv, not -40 Sv. This is probably due to the slowness of the barotropic response relative to the baroclinic at low latitudes, i.e., the density front spreads out before the barotropic adjustment can proceed very far and as the density front spreads, the forcing for the barotropic motion diminishes with ρ_x in Eq. (16).

The average kinetic energy per unit volume in the channel is shown as dashed lines in Fig. 8 for Experiments 2A and 2B (where in reality the kinetic energy is concentrated in the eastern half of the channel, especially in 2A). Comparing the solid curves with the dashed curves in Fig. 8 (i.e., 1A with 2A and 1B with 2B), we note that 1) far more of the potential energy in the initial front is transformed to kinetic energy when bottom topography is present and 2) the inertial oscillations are much less significant in the cases with topography.

4. Discussion and application

Our use of a coarse-grid numerical model to study the Rossby adjustment problem incorporates many

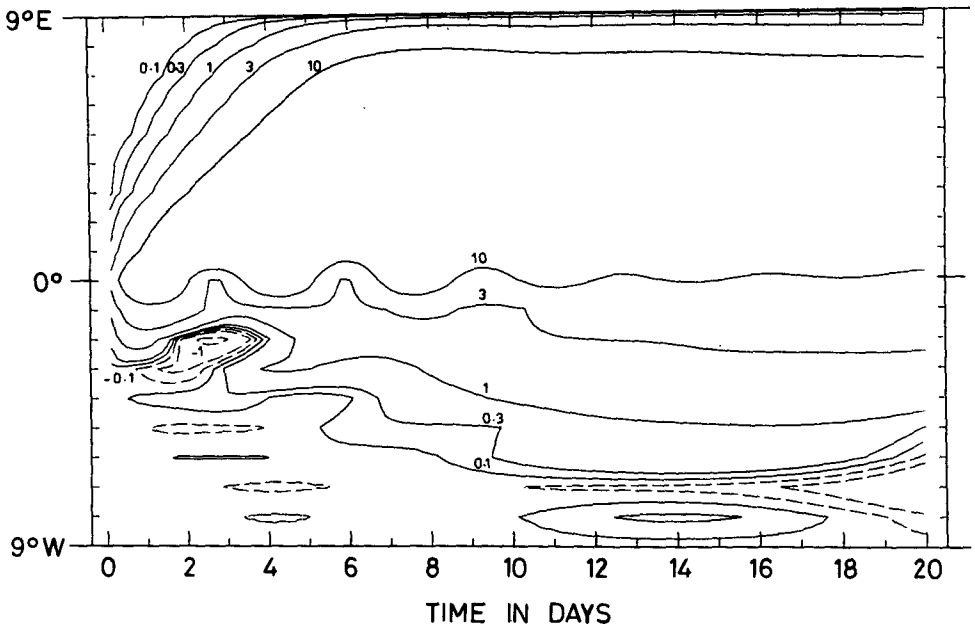

FIG. 13. Space–time contour plot of u (at top level) along the south coast in Experiment 2B (low latitude, with shelf).

new effects, but at the same time, suffers from the many artifacts of numerical models. The large lateral viscosity required for computational stability and the finite grid-resolution in numerical models produce waves that can have very different properties from the inviscid analytic solutions. Worse, different classes of waves are distorted to different extents by the numerical effects. Hsieh *et al.* (1983) showed that baroclinic Kelvin waves can be seriously distorted. For instance, the theoretical phase speed is ~ 2 m s^{-1}, whereas the ob-

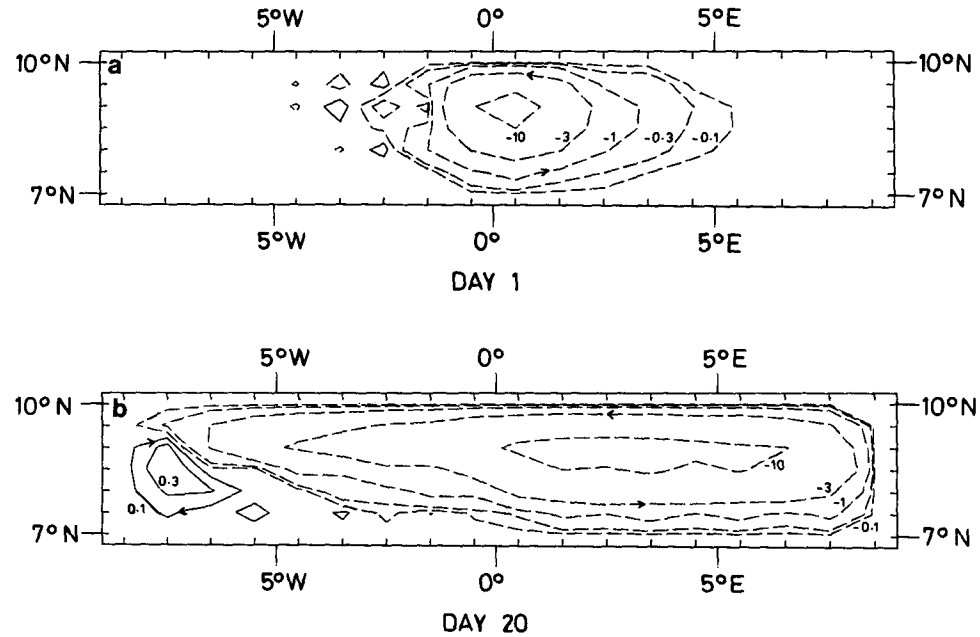

FIG. 14. The streamfunction ψ at (a) day 1 and (b) day 20 in Experiment 2B.

served Kelvin wave speed is 0.22 m s^{-1} in Experiment 1A and 1.0 m s^{-1} in Experiment 1B (where the resolution is better due to a larger Rossby radius). In contrast, the observed shelf-wave phase speeds agree well with the theoretical values.

The speeds of the shelf waves and the baroclinic Kelvin waves are crucial in determining whether the barotropic adjustment proceeds faster or slower than the baroclinic adjustment. At middle to high latitudes, the first-mode shelf-wave speed is typically 3–10 m s^{-1} depending on the shape of the shelf, while the first-mode baroclinic Kelvin-wave speed is ~2 m s^{-1}. At low latitudes, the Kelvin-wave speed is not changed, but the shelf-wave speed decreases with f (c tends to be directly proportional to f). Thus, at low enough latitudes, the baroclinic Kelvin wave travels faster than the shelf wave. The substantially slower Kelvin wave in our numerical model leads to a much slower baroclinic adjustment.

In laboratory models, instabilities often develop from a front (see, e.g., Griffiths and Linden, 1982 or Stern *et al.*, 1982). In our numerical runs, the use of viscosity to control computational instabilities may also adversely suppress the growth of some physical instabilities.

With oceans full of disturbances and fronts, the Rossby adjustment problem evidently has many applications. Here we briefly describe a calculation done using the real topography of the Norwegian–Greenland Sea and the North Atlantic, but closed off with vertical walls as shown in Fig. 15. A shallow sill extending from the United Kingdom through Iceland to Greenland effectively subdivides the region into two basins. We place a "dam" along the sill, with different water masses on the two sides. A stratification corresponding to that observed in winter Atlantic at 70°N, 0°E is assumed for the entire northern basin, while one at 50°N, 20°W is assumed for the southern basin. For this run, the Bryan–Cox model has six vertical levels at 50, 300, 750, 1500, 2500 and 4000 m. Fig. 15 shows the density change (from the initial value) at level 2 (300 m) after 140 days of relaxation without any forcing. An adjustment along the Norwegian coast can clearly be seen. The asymmetry between north and south may be quite important in this region, although much more detailed experiments than are reported here would be needed to study this problem.

5. Summary

We have studied the Rossby adjustment problem in a channel with the Bryan–Cox numerical model. An initial sharp density front was allowed to relax naturally, with the front widening gradually (to a width characterized by the baroclinic Rossby radius when the channel is wide). Because of the larger Rossby radius at low latitudes, more of the initial potential energy of the front is transformed to kinetic energy, thereby producing a stronger response at low latitudes.

The presence of sloping bottom topography in the form of a continental shelf along a boundary introduces a strong barotropic response propagating as a shelf-

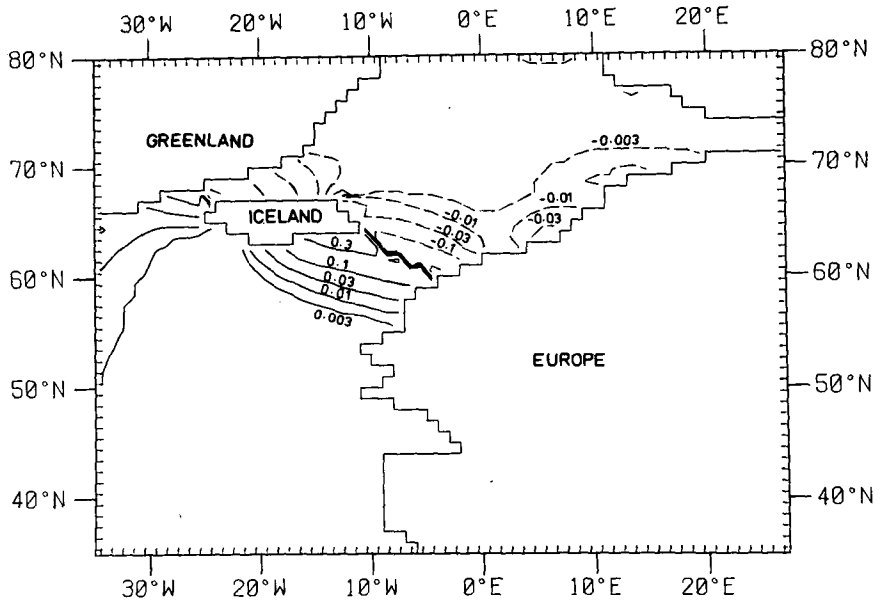

FIG. 15. Density change at level 2 (300 m depth) at day 140 in a 1° × 1° model for the Norwegian Sea where a density front from the United Kingdom to Greenland is allowed to relax without forcing. The model has a solid no-slip boundary.

wave front, behind which a steady barotropic circulation is established. At high latitudes, the barotropic adjustment proceeds much faster than the baroclinic one because shelf waves propagate faster. At low latitudes, the shelf-wave speed, being proportional to f, is much lower and can be less than the baroclinic Kelvin-wave speed. In general, the response is predominantly baroclinic in the absence of topography, but when topography is present, a bottom pressure-torque mechanism drives the so-called "barotropic" or vertically integrated flow, which can release potential energy.

Two interesting nonlinear phenomena were observed in our models 1) the baroclinic Kelvin wave generating a barotropic Rossby wave and 2) internal Poincaré waves of near-inertial frequency transferring energy to subharmonic shelf-waves with $\omega \approx \frac{1}{2}f$. In the latter interaction, a short shelf wave with group velocity opposite to its phase velocity was clearly seen. It is interesting to note that these nonlinear interactions not only transfer energy between baroclinic and barotropic motion, but also between first and second class waves (i.e., gravity and "vorticity" waves).

Our use of a numerical model introduces effects of viscosity and finite grid-resolution. In the flat-bottom channel, a steady alongshore density or pressure gradient is maintained by viscosity after the passage of the baroclinic Kelvin-wave front, whereas the alongshore gradient vanishes in the inviscid solution of Gill (1976). Poor offshore resolution and viscosity combine to decrease the speed of the Kelvin wave, whence the speed of baroclinic adjustment. Finally, we emphasize that as our models were run for only 20 days, longer time-scale adjustment processes have not been studied.

Acknowledgments. We thank Allan Davies, Julian Smith and David Webb for their help in running the numerical model on the CRAY computer at Daresbury Laboratory. The first author was supported in Cambridge by a post-doctoral fellowship from the Natural Sciences and Engineering Research Council of Canada.

REFERENCES

Barton, N. G., 1977: Resonant interactions of shelf waves with wind-generated effects. *Geophys. Astrophys. Fluid Dyn.*, **9**, 101–114.

Davey, M. K., W. W. Hsieh and R. C. Wajsowicz, 1983: The free Kelvin wave with lateral and vertical viscosity. *J. Phys. Oceanogr.*, **13**, 2182–2191.

Gill, A. E., 1976: Adjustment under gravity in a rotating channel. *J. Fluid Mech.*, **77**, 603–621.

——, 1982: *Atmosphere-Ocean Dynamics.* Academic Press, 662 pp.

—— and K. Bryan, 1971: Effects of geometry on the circulation of a three-dimensional southern-hemisphere ocean model. *Deep-Sea Res.*, **18**, 685–721.

——, and E. H. Schumann, 1974: The generation of long shelf waves by the wind. *J. Phys. Oceanogr.*, **4**, 83–90.

Griffiths, R. W., and P. F. Linden, 1982: Laboratory experiments on fronts. Part I: Density-driven boundary currents. *Geophys. Astrophys. Fluid Dyn.*, **19**, 159–187.

Guza, R. T., and R. E. Davis, 1974: Excitation of edge waves by waves incident on a beach. *J. Geophys. Res.*, **79**, 1285–1291.

—— and A. J. Bowen, 1975: The resonant instabilities of long waves obliquely incident on a beach. *J. Geophys. Res.*, **80**, 4529–4534.

—— and D. L. Inman, 1975: Edge waves and beach cusps. *J. Geophys. Res.*, **80**, 2997–3012.

Holland, W. R., 1973: Baroclinic and topographic influences on the transport in western boundary currents. *Geophys. Fluid Dyn.*, **4**, 187–210.

Hsieh, W. W., 1982: Observations of continental shelf waves off Oregon and Washington. *J. Phys. Oceanogr.*, **12**, 887–896.

——, and L. A. Mysak, 1980: Resonant interactions between shelf waves, with applications to the Oregon shelf. *J. Phys. Oceanogr.*, **10**, 1729–1741.

——, M. K. Davey and R. C. Wajsowicz, 1983: The free Kelvin wave in finite-difference numerical models. *J. Phys. Oceanogr.*, **13**, 1383–1397.

LeBlond, P. H., and L. A. Mysak, 1978: *Waves in the Ocean.* Elsevier, 602 pp.

Rossby, C. G., 1937: On the mutual adjustment of pressure and velocity distributions in certain simple current systems: I. *J. Mar. Res.*, **1**, 15–28.

——, 1938: On the mutual adjustment of pressure and velocity distributions in certain simple current systems: II. *J. Mar. Res.*, **2**, 239–263.

Semtner, A. J., 1974: An oceanic general circulation model with bottom topography. Numerical simulation of Weather and Climate, Tech. Rep. No. 9, University of California, Los Angeles, 99 pp.

Stern, M. E., J. A. Whitehead and B.-L. Hua, 1982: The intrusion of a density current along the coast of a rotating fluid. *J. Fluid Mech.*, **123**, 237–265.